RESEARCH ARTICLE

QUANTUM OPTICS

Observation of millihertz-level cooperative Lamb shifts in an optical atomic clock

Ross B. Hutson^{1,2}*, William R. Milner^{1,2}, Lingfeng Yan^{1,2}, Jun Ye^{1,2}*, Christian Sanner³

Collective couplings of atomic dipoles to a shared electromagnetic environment produce a wide range of many-body phenomena. We report on the direct observation of resonant electric dipole-dipole interactions in a cubic array of atoms in the many-excitation limit. The interactions produce spatially dependent cooperative Lamb shifts when spectroscopically interrogating the millihertz-wide optical clock transition in strontium-87. We show that the ensemble-averaged shifts can be suppressed below the level of evaluated systematic uncertainties for optical atomic clocks. Additionally, we demonstrate that excitation of the atomic dipoles near a Bragg angle can enhance these effects by nearly an order of magnitude compared with nonresonant geometries. Our work demonstrates a platform for precise studies of the quantum many-body physics of spins with long-range interactions mediated by propagating photons.

tudies of quantum many-body physics naturally arise in the context of quantum sensing. For any quantum sensor, the amount of extractable information regarding a metrological quantity of interest is fundamentally limited by the number of accessible qubits (1, 2). This creates a generic incentive to build devices capable of manipulating and characterizing quantum systems of ever-increasing size (3-5). Because interactions within the system or with the environment typically scale with system size, the main challenges are then twofold: How can interactions be controlled to reduce systematic effects, and/or how can they be leveraged to generate useful entanglement?

In the context of atomic clocks, notable progress toward probing larger numbers of atoms while avoiding systematic effects resulting from contact interactions has been made by trapping atoms in three-dimensional (3D) optical lattices with at most one atom per lattice site (6–9). Nonetheless, clock shifts caused by long-range resonant dipole-dipole interactions have loomed just beyond experimental detectability (10–12).

The classical electric field, evaluated at a position \mathbf{b} , generated by a point dipole $\mathbf{d_a} \propto e^{-\mathrm{i}\omega t}$, oscillating at an angular frequency ω , and localized at a position \mathbf{a} , is given by $\mathbf{E_a}(\mathbf{b}) = k^3 e^{\mathrm{i}kr} \left\{ [\mathbf{d_a} - \hat{\mathbf{r}} (\hat{\mathbf{r}} \cdot \mathbf{d_a})]/(kr) + [3\hat{\mathbf{r}} (\hat{\mathbf{r}} \cdot \mathbf{d_a}) - \mathbf{d_a}][1/(kr)^3 - \mathrm{i}/(kr)^2]\right\}/4\pi\epsilon_0$, where $\mathbf{r} = \mathbf{r_{ba}} = \mathbf{b} - \mathbf{a}$, $\mathbf{r} = |\mathbf{r}|$, $\hat{\mathbf{r}} = \mathbf{r}/\mathbf{r}$, ϵ_0 is the vacuum permittivity, and $k = \omega/c$ with c being the speed of light (13). A second, freely oscillating dipole $\mathbf{d_b}$ localized at position \mathbf{b} will then dynamically evolve according to the interaction term $H_{\mathbf{ba}} = -\mathbf{d_b} \cdot \mathbf{E_a}(\mathbf{b})$, whose real and imaginary parts, respectively, lead to a frequency shift and damping of the initial excitation. These interactions form the basis of classical linear optics (13–15).

An ensemble of indistinguishable (pseudo-)spin- $\frac{1}{2}$ systems, with internal ground and excited

states labeled $|g\rangle$ and $|e\rangle$, respectively, can analogously be described using the formalism of quantum optics, where the reduced density matrix $\hat{\rho}$ evolves in time t according to the master equation $\partial_t \hat{\rho} = \mathcal{L}_{\text{fixe}}[\hat{\rho}] = \mathcal{L}_1[\hat{\rho}] + \mathcal{L}_2[\hat{\rho}]$ with the Liouvillian superoperator describing collective electromagnetic interactions given in Lindblad form as (16)

$$\mathcal{L}_{2}[\hat{\rho}] = -i \sum_{\mathbf{a}, \mathbf{b}} V_{\mathbf{b} \mathbf{a}} \left(\hat{S}_{\mathbf{b}}^{\dagger} \hat{S}_{\mathbf{a}} \hat{\rho} - \hat{S}_{\mathbf{a}} \hat{\rho} \hat{S}_{\mathbf{b}}^{\dagger} \right) + \text{H.c.}$$
(1)

and generic single-spin dynamics governed by $\mathcal{L}_1[\hat{\rho}]$. Here, $\hat{S}^{+}_{\mathbf{a}} = \zeta^*_{\mathbf{a}}|e\rangle_{\mathbf{a}}\langle g|_{\mathbf{a}}$ is the raising operator for the spin at \mathbf{a} , with $\zeta_{\mathbf{a}}$ being an arbitrary phase factor satisfying $|\zeta_{\mathbf{a}}|^2 = 1$. The coefficients $V_{\mathbf{ba}}$ of the effective Hamiltonian $\hbar \sum_{\mathbf{a},\mathbf{b}} V_{\mathbf{ba}} \hat{S}^{+}_{\mathbf{b}} \hat{S}_{\mathbf{a}} + \text{H.c.}$, where \hbar is the reduced Planck constant, are obtained by quantizing the dipole moments $\mathbf{d_a} \rightarrow \langle g|\hat{\mathbf{d}}|e\rangle \zeta_{\mathbf{a}} \hat{S}^{+}_{\mathbf{a}} + \text{H.c.}$ appearing in the classical interaction terms $H_{\mathbf{ba}}$, applying the rotating wave approximation, and negating the homogeneous self-interaction energy (Lamb shift) $\text{Re}(V_{\mathbf{aa}}) \rightarrow 0$. The characteristic energy scale of \mathcal{L}_2 is set by the excited-state spontaneous decay rate $\Gamma = -2\text{Im}(V_{\mathbf{aa}})$, which is on the order of $2\pi \times 1$ mHz for the clock transition in neutral strontium-87.

Equation 1 has long been known to contain the physics of cooperative decay (17) and cooperative Lamb shifts (18, 19), with these effects being subsequently observed in a wide variety of physical systems (20–38). However, in the context of optical frequency metrology, resonant dipole-dipole interactions are typically neglected because of the relatively low atomic densities and weak transition strengths.

¹JILA, NIST, and University of Colorado, Boulder, CO 80309, USA. ²Department of Physics, University of Colorado, Boulder, CO 80309, USA. ³Department of Physics, Colorado State University, Fort Collins, CO 80523, USA.

*Corresponding author. Email: ross.hutson@colorado.edu (R.B.H.); jun.ye@colorado.edu (J.Y.)

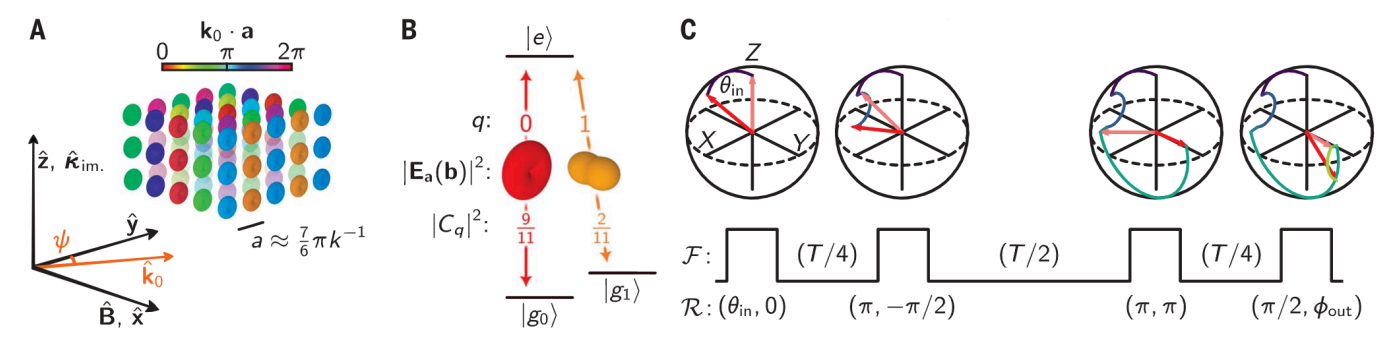


Fig. 1. Experimental setup. (**A**) Atomic dipoles on a cubic lattice, indexed by their positions **a**, are excited with spatially dependent phases $\mathbf{k}_0 \cdot \mathbf{a}$. Proximity to the Bragg condition $\mathbf{k}_0 \cdot \mathbf{a} \hat{\mathbf{y}} = \pi$ leads to long-range phase ordering along the $\hat{\mathbf{y}}$ axis. (**B**) Far-field $(kr_{\mathbf{ba}} \gg 1)$ single-atom radiation patterns $|\mathbf{E}_{\mathbf{a}}(\mathbf{b})|^2$ for the two $(q \in \{0,1\})$ spectroscopically resolved $|e\rangle \leftrightarrow |g_q\rangle$ transitions. (**C**) Resonant laser pulses $\mathcal{R}(\theta, \phi)$ rotate the atomic states by an angle θ about the $(X_{\mathbf{a}}\cos\phi + Y_{\mathbf{a}}\sin\phi)$ axis. The various pulses and free-evolution periods $\mathcal{F}(t)$ are chosen such that the output-state projection $\langle \hat{Z}_{\mathbf{a}}\mathcal{U} \rangle$ is proportional only to terms in $\mathcal{L}_{\text{free}}$ that scale antisymmetrically with $\cos\theta_{\text{in}}$, namely those caused by the resonant dipole-dipole interactions in \mathcal{L}_2 .

Experimental approach for observing cooperative Lamb shifts

We have observed that such interactions cannot always be neglected in an atomic clock. We performed Ramsey spectroscopy on a quantum-degenerate Fermi gas of neutral strontium-87 in a cubic optical lattice with a total free-evolution period of T=2 s. Subsequently imaging the Ramsey interferometer output, the observed population differences served as a proxy for spatially inhomogeneous "clock shifts" of the atomic resonance. Our model, based on the resonant dipole-dipole interactions contained in Eq. 1, accurately reproduces the observed shifts over a wide range of external control parameters.

The spatial distribution of the interferometer signal is shown to be dependent on the relative drive phases and radiation patterns of the atomic dipoles, which we control by varying the angle of incidence of the probe laser and polarization q of the probe photons, respectively. Additionally, the shifts are shown to scale with the strengths of the atomic dipole moments through changes in the pulse area of the initial interferometer pulse and the relative strength of the probed transition. Despite the presence of a relatively large technical dephasing rate $\gamma \approx 2\pi \times 34$ mHz $\gg \Gamma$ caused by Raman scattering of optical lattice photons (39), we relied on the precision of the atomic clock to divide a Ramsey fringe by more than a part in 10³ to measure millihertz-level cooperative Lamb shifts in the limit $\Gamma T \ll 1$ over a wide range of initial excitation fractions.

Viewed in the context of modern quantum optics (10, 40-46), periodic arrays of atomic dipoles are a promising platform for studies of many-body physics because they are thought to host a rich Hilbert space containing longlived quasiparticles (44, 45, 47). Although cooperative Lamb shifts in the multiple-excitation limit have recently been observed, modeling of the observed shift was unsuccessful because decoherence mechanisms that significantly affect the dynamics at long interrogation times $\Gamma t \gg 1$ were not accounted for (48). Our work suggests that optical atomic clocks are natural platforms for studies of many-body quantum optics given that all parameters contained in \mathcal{L}_{free} are systematically characterized, and coherent manipulations and projective measurements on timescales much shorter than Γ^{-1} are readily achievable.

Experimental overview and optical spectroscopy

As previously described (49, 50) and schematically represented in Fig. 1A, in a shot-based experiment with a cycle time of 12.5 s, a single-component Fermi-degenerate gas of $N_{\rm tot} \approx 10^4$ strontium-87 atoms is loaded into the ground band of a cubic optical lattice and initialized into the $|e\rangle = |5s5p^3P_0, F = 9/2, m_F = -9/2\rangle$ electronic state. The optical lattice is formed

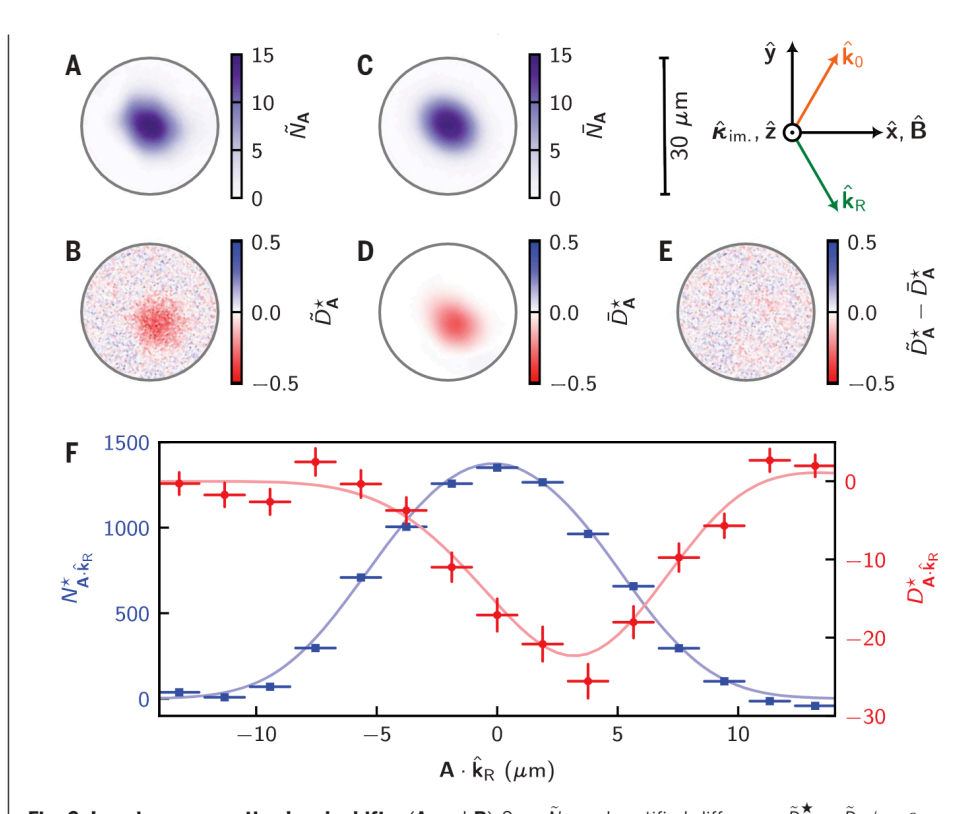


Fig. 2. Imaging cooperative Lamb shifts. (A and B) Sum \tilde{N}_A and rectified difference $\tilde{D}_A^{\bigstar} = \tilde{D}_A/\cos\theta_{\rm in}$ signals averaged over the subset of data corresponding to the angular momentum preserving the q=0 transition and resonant angle of incidence $\psi=29.5^\circ$. Deviations of \tilde{D}_A^{\bigstar} from zero indicate the presence of clock shifts that scale antisymmetrically with $\cos\theta_{\rm in}$; the differences in the spatial profiles of \tilde{N}_A and \tilde{D}_A^{\bigstar} indicate the presence of long-range, anisotropic interactions. (**C** and **D**) The modeled sum signal \bar{N}_A (C) is obtained by fitting \tilde{N}_A to a Fermi-Dirac distribution, which is then fed into Eq. 2 to obtain the modeled difference signal \bar{D}_A (D) using no other free parameters (51). (**E**) The residuals of the subtraction $\tilde{D}_A^{\bigstar} - \bar{D}_A^{\bigstar}$. The maximum of D_A^{\bigstar} is spatially offset from the maximum of N_A along the direction $\hat{k}_R = \hat{k}_0 - 2(\hat{k}_0 \cdot \hat{y})\hat{y}$ owing to constructive interference of the reflected probe light along k_R . (**F**) 1D projections of the sum $N_{A\cdot\hat{k}_R}$ and rectified difference $D_{A\cdot\hat{k}_R}^{\bigstar}$ signals are obtained by projecting the images in (A) to (D) onto \hat{k}_R . The measured signals $\tilde{N}_{A\cdot\hat{k}_R}$ and $\tilde{D}_{A\cdot\hat{k}_R}^{\bigstar}$ are shown as blue circles and red squares, respectively. Vertical error bars represent 1σ standard errors, and horizontal bars show the 2-μm binwidth of the projections onto \hat{k}_R . The modeled signals $\tilde{N}_{A\cdot\hat{k}_R}$ are shown as blue and red lines, respectively.

with a lattice constant of $a_{\rm lat}\approx 407$ nm by interfering retro-reflected Gaussian laser beams, with 60-µm $1/e^2$ radii and peak depths of $k_{\rm B}\times 12$ µK (where $k_{\rm B}$ is the Boltzmann constant), along each of the $\hat{\bf x}$, $\hat{\bf y}$, and $\hat{\bf z}$ axes. At these depths, tunneling rates are ~10 mHz between neighboring sites. Indexing the lattice sites by their positions ${\bf a}=a_{\rm lat}(x\hat{\bf x}+y\hat{\bf y}+z\hat{\bf z})$ for integer $\{x,y,z\}$, in situ tomographic imaging (50) allows for the reconstruction of the sitewise atomic filling fractions $n_{\bf a}$, revealing a Fermi-Dirac distribution with a fitted peak density of $n_0\approx 0.80$, root mean square (RMS) radii of $(w_{\hat{\bf x}'},w_{\hat{\bf y}'},w_{\hat{\bf z}'})\approx (3.4\,\mu{\rm m},4.3\,\mu{\rm m},2.4\,\mu{\rm m})$, and a mean entropy per atom of $2.0\times k_{\rm B}$ (51).

Clock spectroscopy is then performed on the $5s^2{}^1S_0 \leftrightarrow 5s5p{}^3P_0$ so-called clock transition at $v=kc/2\pi \approx 429$ THz using laser light that is phase stabilized to a cryogenic-silicon optical cavity (9,52). The probe light propagates with

a wave-vector $\mathbf{k}_0 = k(\hat{\mathbf{x}}\sin\psi + \hat{\mathbf{y}}\cos\psi)$, motivating the choice of local frame $\zeta_{\mathbf{a}} = e^{-\mathrm{i}(\omega t - \mathbf{k}_0 \cdot \mathbf{a})}$. Resonant pulses with a $2\pi \times 50$ Hz Rabi frequency, and variable pulse areas θ and phase shifts ϕ , perform global rotations of the atomic state $\hat{\rho} \rightarrow \mathcal{R}(\theta, \phi) \hat{\rho} = \exp\left[-i\theta \sum_{\mathbf{a}} (\hat{S}_{\mathbf{a}}^{^{\mathsf{T}}} e^{-i\phi} + \right]$ $\hat{S}_{\mathbf{a}}e^{\mathrm{i}\phi}/2|\hat{\rho} + \text{H.c.}$. A homogeneous $B \approx 290 \,\mu\text{T}$ magnetic field applied along the $\hat{\mathbf{x}}$ axis creates a 540-Hz differential Zeeman splitting between the two available ground states, $|g_q\rangle = |5s^{21}S_0|$, $F = 9/2, m_F = -9/2 + q$ for $q \in \{0, 1\}$ representing the polarization of an absorbed photon in the spherical basis such that their respective resonances with the excited state are spectroscopically resolved. As represented in Fig. 1B, each subspace exhibits distinct far-field $(kr_{\mathbf{ba}} \gg 1)$ radiation patterns $|\mathbf{E_a}(\mathbf{b})|^2$ owing to differences in the magnitudes C_q ($C_0 = \sqrt{9/11}$ and $C_1 =$ $\sqrt{2/11}$) and orientations \mathbf{e}_a [$\mathbf{e}_0 = \hat{\mathbf{x}}$ and $\mathbf{e}_1 = \hat{\mathbf{e}}_0$ $(\hat{\mathbf{y}} - i\hat{\mathbf{z}})/\sqrt{2}$] of the atomic dipole moments

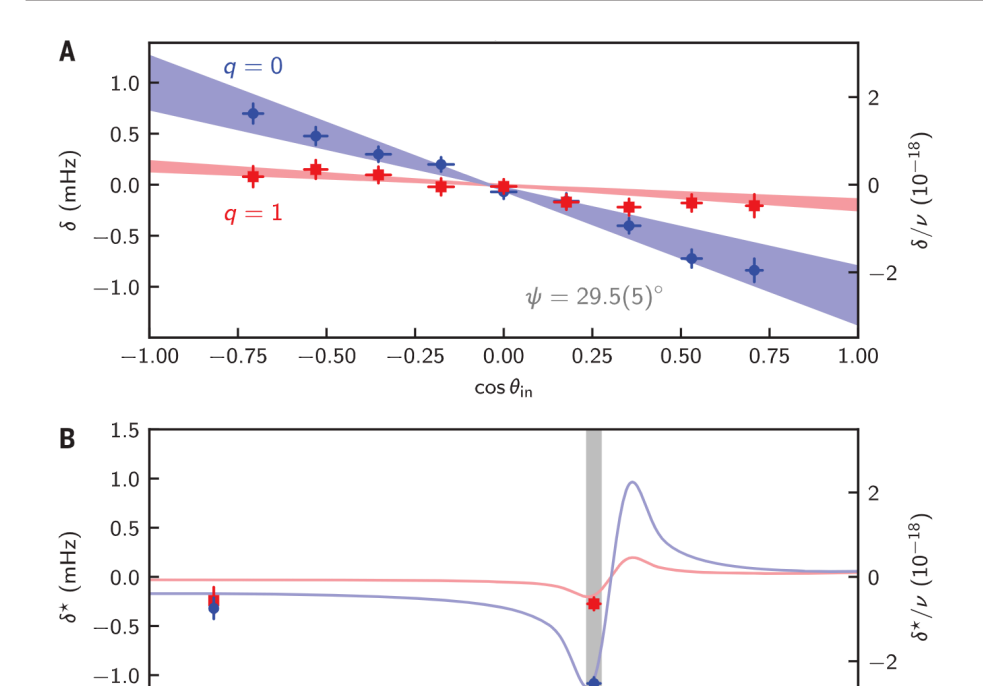


Fig. 3. Controlling cooperative Lamb shifts. (A) Scaling of the ensemble-averaged shift δ versus the initial spin projection $\cos\theta_{\text{in}}$ for $\psi=29.5(5)^{\circ}$ and both q=0 (blue) and q=1 (red). Data points show the measured shifts $\bar{\delta}$, with vertical error bars representing 1σ standard errors and horizontal error bars representing 2% observed fluctuations in the initial pulse area θ_{in} . Shaded regions show the modeled shifts $\bar{\delta}$, propagating the experimental uncertainties in ψ and θ_{in} . (B) Angle-of-incidence dependence of the shift sensitivity $\delta^*=\delta/\cos\theta_{\text{in}}$ to changes in the initial spin projection. Data points and solid lines show the measured and modeled shift sensitivities, respectively. The vertical gray bar represents the angle of incidence used in (A).

 ψ (degrees)

20

30

 $\langle e|\hat{\mathbf{d}}|g_q\rangle=dC_q\mathbf{e}_q$ (12), where d^2 is proportional to the excited state's natural decay rate $\Gamma=k^3d^2/3\pi\epsilon_0\hbar=2\pi\times 1.35(3)\mathrm{mHz}$ (53). For each angle of incidence, the polarization of the probe laser is adjusted to obtain roughly equal Rabi coupling strengths for each transition at fixed intensity.

-1.5

0

10

Figure 1C depicts the time evolution of the atomic state, as represented on the Bloch sphere with vector components $\hat{X}_{\mathbf{a}} = \hat{S}^{\dagger}_{\mathbf{a}} + \hat{S}_{\mathbf{a}}$, $\hat{Y}_{\mathbf{a}} = -\mathrm{i}(\hat{S}^{\dagger}_{\mathbf{a}} - \hat{S}_{\mathbf{a}})$, and $\hat{Z}_{\mathbf{a}} = \hat{S}^{\dagger}_{\mathbf{a}} \hat{S}_{\mathbf{a}} - \hat{S}_{\mathbf{a}} \hat{S}^{\dagger}_{\mathbf{a}}$ throughout the spectroscopic sequence \mathcal{U} . Starting with the initial conditions $\langle \hat{S}^{\dagger}_{\mathbf{a}} \hat{S}_{\mathbf{a}} \rangle = n_{\mathbf{a}}$ and $\langle \hat{S}_{\mathbf{a}} \hat{S}^{\dagger}_{\mathbf{a}} \rangle = 0$, the first pulse $\mathcal{R}(\theta_{\mathrm{in}}, 0)$ rotates the population imbalance of the atomic state $\langle \hat{Z}_{\mathbf{a}} \rangle \rightarrow n_{\mathbf{a}} \cos \theta_{\mathrm{in}}$. The elastic contribution of \mathcal{L}_2 to the subsequent free-evolution $\mathcal{F}(t) = \mathrm{e}^{\mathcal{L}_{\mathrm{free}}t}$ can be intuited, for short times $\Gamma t \ll 1$, as an Ising-type interaction that rotates each atom's Bloch vector about the $Z_{\mathbf{a}}$ axis at a rate of $-\cos \theta_{\mathrm{in}} \sum_{\mathbf{b}} n_{\mathbf{b}} n_{\mathbf{a}} \mathrm{Re}(V^*_{\mathbf{ba}})$. The two "spin-echo" pulses $\mathcal{R}(\pi, \phi)$ preserve

The two "spin-echo" pulses $\mathcal{R}(\pi,\phi)$ preserve the coherent dynamics generated by \mathcal{L}_2 while suppressing the various single-particle dephasing mechanisms contained in $\mathcal{L}_1[\hat{\rho}] = -i\sum_{\mathbf{a}}(\Delta\omega_{\mathbf{a}}-i\gamma/2)(\hat{S}_{\mathbf{a}}^{\dagger}\hat{S}_{\mathbf{a}}\hat{\rho}-\hat{S}_{\mathbf{a}}\hat{\rho}\hat{S}_{\mathbf{a}}^{\dagger}) + \text{H.c.}$, where $\Delta\omega_{\mathbf{a}}$ is the relative detuning of atom \mathbf{a} with respect to the probe laser. The domi-

nant contribution to $\Delta \omega_{\mathbf{a}}$ arises from frequency drifts of the probe laser on the order of 1 Hz between daily measurements of the transition resonance frequencies. Differential ac Stark shifts varying with the local lattice intensity also contribute to $\Delta \omega_{\mathbf{a}}$ yet are limited to the

40

50

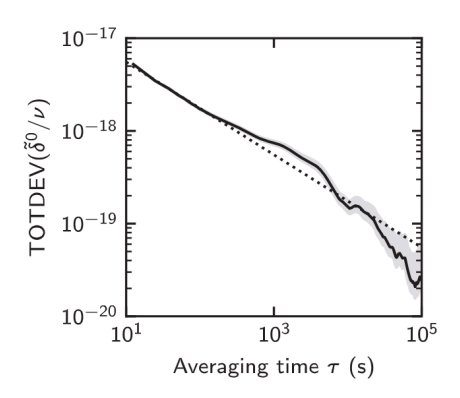


Fig. 4. Instability of clock shift evaluation. The solid black line shows the total deviation (TOTDEV) (62) of the spin-balanced clock shift $\tilde{\delta}^0/\nu$ as a function of averaging time $\tau.$ The shaded region shows the 1σ confidence interval. The dotted black line shows a fit to the data for $\tau < 100$ s, assuming a white noise floor.

sub–10-mHz level by optimizing the optical frequency of each trapping beam (7). These detunings do not directly affect the final state because the spin-echo pulses anticommute with time evolution under \mathcal{L}_1 in the limit $\gamma \to 0$, whereas the spin-echo pulses approximately commute with evolution under \mathcal{L}_2 for $\Gamma t \ll 1$. Finite γ leads to a decay in both the singleatom coherences $\langle \hat{S}^{\dagger}_{\mathbf{a}} \rangle \simeq e^{-\gamma t/2}$ and excited state populations $\langle \hat{S}^{\dagger}_{\mathbf{a}} \hat{S}_{\mathbf{a}} \rangle \simeq e^{-\gamma t}$. For an increasing number of spin-echo pulses, the time-averaged longitudinal decay asymptotically approaches $\langle \hat{Z}_{\mathbf{a}} \rangle \simeq e^{-\gamma t/2}$. The final $\mathcal{R}(\pi/2,\phi_{\text{out}})$ pulse maps the interaction-induced phase shifts of the coherences onto the difference in electronic populations.

A diffraction-limited imaging system with a 1.3- μ m 1/ e^2 resolution then records the columnintegrated populations of the ground $\tilde{N}_{\mathbf{A}}^{g}$ and excited $\tilde{N}_{\mathbf{A}}^{e}$ states onto a scientific complementary metal oxide semiconductor (sCMOS) camera through absorption imaging along $\mathbf{\kappa}_{\text{im.}} = \hat{\mathbf{z}}$ (8, 51). Here, **A** indexes the sensor pixels by their positions. Although the collective spin vector does not necessarily evolve linearly in time when subject to Eq. 1 (10, 12), the ensemble-averaged frequency shift may be computed, in the limit of small acquired phase shifts, as $\tilde{\delta} = (2\pi T)^{-1} \sum_{\mathbf{A}} \tilde{D}_{\mathbf{A}} / \sum_{\mathbf{A}} \tilde{N}_{\mathbf{A}}$, where $\tilde{N}_{\mathbf{A}} = (\tilde{N}_{\mathbf{A}}^{e} + \tilde{N}_{\mathbf{A}}^{g})$ and $\tilde{D}_{\mathbf{A}} = (\tilde{N}_{\mathbf{A}}^{e} - \tilde{N}_{\mathbf{A}}^{g}) / \mathcal{C}$ are the sum and difference signals, respectively, and $\mathcal{C} = \sin(\theta_{\text{in}})\sin(\phi_{\text{out}})e^{-\gamma T/2}$ is the interferometric sensitivity. Approximately 10⁴ experimental shots were recorded over a period of 2 weeks while independently modulating the four parameters: $\sin \phi_{\text{out}} \in \{-1, 1\}, \cos \theta_{\text{in}} \in [-1/\sqrt{2}, 1/\sqrt{2}], q \in \{-1, 1\}, \text{ and } 0 \in [-1/\sqrt{2}, 1/\sqrt{2}], q \in [-1/\sqrt{$ $\{0,1\}$, and $\psi \in \{0^{\circ}, 29.5(5)^{\circ}\}$.

Experimental evidence for cooperative Lamb shifts

We compare experimentally derived quantities (denoted by symbols covered with a tilde, ~) with their modeled equivalents (denoted by symbols covered with a bar, ~) obtained by substituting $\tilde{N}_{\mathbf{A}}^g \to \bar{N}_{\mathbf{A}}^g = \sum_{\mathbf{a} \parallel \mathbf{A}} (n_{\mathbf{a}} - \langle \hat{Z}_{\mathbf{a}} \mathcal{U} \rangle)/2$ and $\tilde{N}_{\mathbf{A}}^e \to \bar{N}_{\mathbf{A}}^e = \sum_{\mathbf{a} \parallel \mathbf{A}} (n_{\mathbf{a}} + \langle \hat{Z}_{\mathbf{a}} \mathcal{U} \rangle)/2$, where $\mathbf{a} \parallel \mathbf{A}$ denotes the set of all atoms whose image is projected onto the pixel \mathbf{A} , and the expectation value of $\hat{Z}_{\mathbf{a}}$ at the output of the interferometer is computed as

$$\begin{split} & \left\langle \hat{Z}_{\mathbf{a}} \mathcal{U} \right\rangle = n_{\mathbf{a}} \mathcal{C}[J_{\mathbf{a}} \cos(\Phi) + (1 - K_{\mathbf{a}}) \sin(\Phi)] \\ & J_{\mathbf{a}} = -\cos(\theta_{\mathrm{in}}) T \sum_{\mathbf{b} \neq \mathbf{a}} n_{\mathbf{b}} \mathrm{Re} \left(V_{\mathbf{b}\mathbf{a}}^{*}\right) + \mathcal{O}\left(\Gamma \gamma T^{2}\right) \\ & K_{\mathbf{a}} = \frac{\Gamma T}{2} + \mathcal{O}\left(\Gamma \gamma T^{2}\right) \end{split} \tag{2}$$

where $J_{\bf a}$ ($K_{\bf a}$) is the leading order, in ΓT , phase-shift (decoherence) of atom $\bf a$ resulting from resonant dipole-dipole interactions with all other atoms and whose full-time dependence in terms of the quantity γT is given in the supplementary materials (51). The parameter $\Phi = \Delta \phi(T) - 2\Delta \phi(3T/4) + 2\Delta \phi(T/4) - \Delta \phi(0)$ results from propagating noise-induced deviations

in the time-dependent relative phase between the atoms and the laser $\phi \rightarrow \phi + \Delta \phi(t)$ evaluated at each of the four rotation pulses.

On timescales comparable to T, the probe laser exhibits white frequency noise, where the RMS difference in phases over a time interval Δt is approximately $\sqrt{\langle \Delta \phi^2(\Delta t) \rangle}/\Delta t \approx 90 \text{ mrads}^{-1}$ (52), contributing a zero-mean, stochastic signal on the order of $\Delta \tilde{D}_{\mathbf{A}} \approx \sqrt{\Phi^2 \tilde{N}_{\mathbf{A}}} \approx \tilde{N}_{\mathbf{A}} \times$ 110 mrad to individual measurements of $\hat{D}_{\mathbf{A}}$ (51). Noise in the observed data is consistent with $\sqrt{\Phi^2} \approx 230$ mrad and 300 mrad for the q = 0 and q = 1 transitions, respectively. We attribute the excess, transition-dependent noise to 3.2-nT (RMS) fluctuations in the magnetic field on timescales comparable to T(9, 51, 54). Owing to differences in the spatial profiles of $\Delta \bar{D}_{\mathbf{A}} \propto n_{\mathbf{a}}$ and $\bar{D}_{\mathbf{A}} \propto n_{\mathbf{a}} J_{\mathbf{a}}$, we are able to remove population differences caused by fluctuations in the probe-laser phase by applying corrections $\tilde{D}_{\mathbf{A}} \rightarrow \tilde{D}_{\mathbf{A}} - \mathcal{P}_{\Delta D}^{\mathrm{opt}} \Delta \bar{D}_{\mathbf{A}}$ to the presented data, where the coefficients $\mathcal{P}_{\Delta D}^{\text{opt}}$ are obtained from least squares fits minimizing the quantity $\sum_{\mathbf{A}} ig(\mathcal{P}_{\Delta D} \Delta ar{D}_{\mathbf{A}} + \mathcal{P}_D ar{D}_{\mathbf{A}} - ilde{D}_{\mathbf{A}}ig)^2/\mathrm{Var}ig(ilde{D}_{\mathbf{A}}ig)$ over the parameters $\mathcal{P}_{\Delta D}$ and \mathcal{P}_{D} (51).

Figure 2 shows the sum $N_{\mathbf{A}}$ and rectified difference $D_{\mathbf{A}}^{\star} = D_{\mathbf{A}}/\cos(\theta_{\mathrm{in}})$ signals averaged over the subset of data with maximal shift sensitivities: $\psi = 29.5^{\circ}$ and q = 0. The ensembleaveraged cooperative Lamb shifts are plotted against $\cos\theta_{\rm in}$ for $\psi=29.5^{\rm o}$ in Fig. 3A. A χ^2 analysis comparing the measured shifts with the model at each set of $(\cos\theta_{\rm in}, q, \psi)$ gives $\chi^2/(22\text{d.o.f.})\approx 1.18$. The shift's sensitivity to $(2\pi T)^{-1} \sum_{\bf A} D_{\bf A}^{\star} / \sum_{\bf A} N_{\bf A}$ is plotted against ψ in Fig. 3B.

Whereas $V_{\mathbf{ba}}$ asymptotically decays with increasing separation as $1/kr_{\mathbf{ba}}$, the contained phase factors $e^{-i(kr_{ba}+\mathbf{k}_0\cdot r_{ba})}$ average to zero for incommensurate $ka_{lat} \approx 7\pi/6$ and $\psi = 0^{\circ}$, resulting in effectively nearest-neighbor interactions scaling with the local filling fractionsi.e., $J_{\mathbf{a}} \propto n_{\mathbf{a}}$. However, the subwavelength lattice spacing $ka_{\rm lat} < 2\pi$ guarantees the unique existence of the Bragg resonance at $\psi =$ $\arccos(\pi/ka_{\text{lat}}) \approx 30.8^{\circ}, \text{ satisfying } \mathbf{k}_0 \cdot a_{\text{lat}} \hat{\mathbf{y}} = \pi$ such that the radiated fields add constructively along $\mathbf{k}_{R} = \mathbf{k}_{0} - 2(\mathbf{k}_{0} \cdot \hat{\mathbf{y}}) \hat{\mathbf{y}}$. Numerically, we find that the ensemble-averaged interaction strengths are maximized, and scale with the system size as $N_{\text{tot}}^{1/3}$, at angular detunings from exact Bragg resonance set by the diffraction limit $\pi/2k(w_{\hat{x}'}^2+w_{\hat{y}'}^2)^{1/2}\approx 1.8^{\circ}$ (10,51,55).

Fitting the observed shifts to $\tilde{\delta} = \tilde{\delta}^* \cos \theta_{\rm in} + \tilde{\delta}^0$, we evaluate the mean clock shift owing to resonant dipole-dipole interactions at $cos\theta_{in}=0$ to be $\tilde{\delta}^0/\nu = -1.3(8)\times 10^{-19},$ which demonstrates that systematic effects can be made negligible relative to the lowest reported total systematic uncertainties for optical atomic clocks (56–58). Figure 4 displays the fractional frequency instability of the $\tilde{\delta}^0/\nu$ evaluation, which exhibits a $1.8 \times 10^{-17} / \sqrt{\text{Hz}}$ short-term white noise floor.

Discussion and outlook

We have performed measurements of, and successfully modeled, cooperative Lamb shifts in a 3D optical lattice clock. Control over the spatial orientations of the probe light and excited dipole moments allow for a notable modification of the magnitude of these effects-from levels relevant to state-of-the-art atomic clocks to more than an order of magnitude below. Technical dephasing caused by Raman scattering of optical lattice photons prevented the study of dynamics beyond $\Gamma t \ll 1$.

It is interesting to consider a regime where collective interactions are significantly stronger than technical dephasing rates. This may be achieved by probing transitions with stronger intrinsic dipole moments, either directly or by optically dressing the clock states (59). Under such conditions, where coherent manipulations on timescales much shorter than dynamics associated with free evolution may still be possible, collective light-matter interactions are expected to lead to spin squeezing (60) and other exotic states of quantum matter (45). The desire to produce metrologically useful entanglement motivates future work interrogating the $5s5p \,^3P_0 \leftrightarrow 5s4d \,^3D_1$ transition at 2.6 µm satisfying $ka_{\text{lat}} \approx 1$ (60, 61), where linearly polarized light incident along $\hat{\mathbf{k}}_0 \cdot \hat{\mathbf{B}} \ll 1$ can produce coherent dynamics that are dominant over collective dissipation. Beyond defining a precise platform for the study of effective photonphoton interactions (44, 45), such engineered arrays of narrow-band quantum emitters provide a path to unexplored photonic devices based on controlled collective atom-photon dynamics.

REFERENCES AND NOTES

- S. L. Braunstein, C. M. Caves, Phys. Rev. Lett. 72, 3439–3443 (1994).
- V. Giovannetti, S. Lloyd, L. Maccone, Phys. Rev. Lett. 96, 010401 (2006)
- C. M. Caves, Phys. Rev. Lett. 45, 75-79 (1980).
- W. M. Itano et al., Phys. Rev. A 47, 3554-3570 (1993).
- M. O. Scully, J. P. Dowling, Phys. Rev. A 48, 3186-3190 (1993).
- T. Akatsuka, M. Takamoto, H. Katori, Phys. Rev. A 81, 023402 (2010).
- S. L. Campbell et al., Science 358, 90-94 (2017)
- G. E. Marti et al., Phys. Rev. Lett. 120, 103201 (2018) E. Oelker et al., Nat. Photonics 13, 714-719 (2019).
- 10. D. E. Chang, J. Ye, M. D. Lukin, Phys. Rev. A 69, 023810 (2004).
- 11. S. Krämer, L. Ostermann, H. Ritsch, Europhys. Lett. 114, 14003
- 12. A. Cidrim et al., Phys. Rev. Lett. 127, 013401 (2021).
- 13. J. D. Jackson, Classical Electrodynamics (Wiley, ed. 3, 1998).
- 14. P. de Vries, D. V. van Coevorden, A. Lagendiik, Rev. Mod. Phys. 70. 447-466 (1998).
- 15. F. Andreoli, M. J. Gullans, A. A. High, A. Browaeys, D. E. Chang, Phys. Rev. X 11, 011026 (2021)
- 16. R. H. Lehmberg, Phys. Rev. A 2, 883-888 (1970).
- R. H. Dicke, Phys. Rev. 93, 99-110 (1954).
- 18. V. M. Fain, Sov. Phys. JETP 9, 562 (1959)
- 19. R. Friedberg, S. Hartmann, J. Manassah, Phys. Rep. 7, 101-179 (1973).
- 20. N. Skribanowitz, I. P. Herman, J. C. MacGillivray, M. S. Feld, Phys. Rev. Lett. 30, 309-312 (1973).
- M. Gross, C. Fabre, P. Pillet, S. Haroche, Phys. Rev. Lett. 36, 1035-1038 (1976)
- 22. M. Gross, P. Goy, C. Fabre, S. Haroche, J. M. Raimond, Phys. Rev. Lett. 43, 343-346 (1979).
- 23. D. Pavolini, A. Crubellier, P. Pillet, L. Cabaret, S. Liberman, Phys. Rev. Lett. 54, 1917-1920 (1985).
- 24. P. V. Zinov'ev et al., Sov. Phys. JETP 58, 1129-1133 (1983).
- 25. O. P. Varnavskii, A. N. Kirkin, A. M. Leontovich, Sov. Phys. JETP **59**, 716 (1984).

- 26. R. G. DeVoe, R. G. Brewer, Phys. Rev. Lett. 76, 2049-2052 (1996).
- 27. M. D. Barnes, P. S. Krstic, P. Kumar, A. Mehta, J. C. Wells, Phys. Rev. B 71, 241303 (2005).
- 28. M. Scheibner et al., Nat. Phys. 3, 106-110 (2007)
- 29. A. Goban et al., Phys. Rev. Lett. 115, 063601 (2015).
- 30. B. H. McGuyer et al., Nat. Phys. 11, 32-36 (2015).
- 31. M. Houde, A. Mathews, F. Rajabi, Mon. Not. R. Astron. Soc. 475,
- 32. W. R. Garrett, R. C. Hart, J. E. Wray, I. Datskou, M. G. Payne, Phys. Rev. Lett. 64, 1717-1720 (1990).
- 33. R. Röhlsberger, K. Schlage, B. Sahoo, S. Couet, R. Rüffer, Science 328, 1248-1251 (2010).
- J. Keaveney et al., Phys. Rev. Lett. 108, 173601 (2012).
- 35. A. F. van Loo et al., Science 342, 1494-1496 (2013).
- 36. Z. Meir, O. Schwartz, E. Shahmoon, D. Oron, R. Ozeri, Phys. Rev. Lett. **113**. 193002 (2014).
- 37. J. Rui et al., Nature 583, 369-374 (2020).
- 38. G. Ferioli, A. Glicenstein, L. Henriet, I. Ferrier-Barbut, A. Browaeys, Phys. Rev. X 11, 021031 (2021).
- 39. R. B. Hutson et al., Phys. Rev. Lett. 123, 123401 (2019).
- 40. H. Zoubi, H. Ritsch, Phys. Rev. A 83, 063831 (2011).
- 41. S. D. Jenkins, J. Ruostekoski, Phys. Rev. A 86, 031602 (2012).
- 42. D. E. Chang, L. Jiang, A. V. Gorshkov, H. J. Kimble, New J. Phys. 14. 063003 (2012).
- 43. R. J. Bettles, S. A. Gardiner, C. S. Adams, Phys. Rev. A 92, 063822
- 44. A. Asenio-Garcia, M. Moreno-Cardoner, A. Albrecht,
- H. J. Kimble, D. E. Chang, Phys. Rev. X 7, 031024 (2017). 45. L. Henriet, J. S. Douglas, D. E. Chang, A. Albrecht, Phys. Rev. A 99, 023802 (2019).
- 46. E. Sierra, S. J. Masson, A. Asenjo-Garcia, Phys. Rev. Res. 4, 023207 (2022)
- 47. Y.-X. Zhang, K. Mølmer, Phys. Rev. Lett. 122, 203605 (2019).
- 48. A. Glicenstein et al., Phys. Rev. Lett. 124, 253602 (2020).
- 49. L. Sonderhouse et al., Nat. Phys. 16, 1216-1221 (2020).
- 50. W. R. Milner, L. Yan, R. B. Hutson, C. Sanner, J. Ye, Phys. Rev. A 107. 063313 (2023)
- 51. See the supplementary materials.
- 52. D. G. Matei et al., Phys. Rev. Lett. 118, 263202 (2017).
- 53. J. A. Muniz, D. J. Young, J. R. K. Cline, J. K. Thompson, Phys. Rev. Res. 3, 023152 (2021).
- 54. M. M. Boyd et al., Phys. Rev. A 76, 022510 (2007).
- 55. J. T. Manassah, Phys. Lett. A 374, 1985-1988 (2010).
- 56. W. F. McGrew et al., Nature 564, 87-90 (2018).
- 57. S. M. Brewer et al., Phys. Rev. Lett. 123, 033201 (2019)
- 58. T. Bothwell et al., Metrologia 56, 065004 (2019).
- 59. R. Santra, E. Arimondo, T. Ido, C. H. Greene, J. Ye, Phys. Rev. Lett. 94. 173002 (2005).
- 60. C. Qu, A. M. Rey, Phys. Rev. A 100, 041602 (2019).
- 61. S. J. Masson, J. P. Covey, S. Will, A. Asenjo-Garcia, Dicke superradiance in ordered arrays of multilevel atoms. arXiv:2304.00093 [quant-ph]
- 62. D. A. Howe, IEEE Trans. Ultrason. Ferroelectr. Freq. Control 47, 1102-1110 (2000).
- 63. R. B. Hutson, W. R. Milner, L. Yan, J. Ye, C. Sanner, Observation of mHz-level cooperative Lamb shifts in an optical atomic clock dataset, Dryad (2023); https://doi.org/10.5061/dryad.wpzgmsbtj.

ACKNOWLEDGMENTS

We thank D. Kedar for technical assistance and D. E. Chang, H. Ritsch, and M. D. Lukin for useful discussions. We also thank S. L. Campbell, N. Darkwah Oppong, A. M. Rey, and D. Wellnitz for careful reading of the manuscript and for providing insightful comments. Funding: Funding for this work is provided by National Science Foundation (NSF) QLCI OMA-2016244, the US Department of Energy Center of Quantum System Accelerator, a V. Bush Fellowship, the National Institute of Standards and Technology (NIST), and NSF Phys-1734006. Author contributions: All authors contributed to carrying out the experiments, interpreting the results, and writing the manuscript. Competing interests: The authors declare no competing interests. Data and materials availability: All data and code used to generate the figures are archived at Dryad (63). License information: Copyright © 2024 the authors, some rights reserved; exclusive

licensee American Association for the Advancement of Science. No claim to original US government works, https://www.science.org/ about/science-licenses-journal-article-reuse

SUPPLEMENTARY MATERIALS

science.org/doi/10.1126/science.adh4477 Supplementary Text Figs. S1 to S4 Tables S1 to S3

Submitted 7 March 2023; accepted 15 December 2023 10.1126/science.adh4477